Tectonophysics 814 (2021) 228944

Contents lists available at ScienceDirect

Tectonophysics

journal homepage: www.elsevier.com/locate/tecto

Yield failure of the subducting plate at the Mariana Trench

Jiangyang Zhang [a,f], Fan Zhang [a,b,c,*], Jian Lin [a,c,d,e,*], Hongfeng Yang [g]

[a] Key Laboratory of Ocean and Marginal Sea Geology, South China Sea Institute of Oceanology, Innovation Academy of South China Sea Ecology and Environmental Engineering, Chinese Academy of Sciences, Guangzhou 510301, China
[b] Southern Marine Science and Engineering Guangdong Laboratory (Guangzhou), Guangzhou 511458, China
[c] China-Pakistan Joint Research Center on Earth Sciences, CAS-HEC, Islamabad 45320, Pakistan
[d] Department of Geology and Geophysics, Woods Hole Oceanographic Institution, Woods Hole, MA 02543, USA
[e] Department of Ocean Science and Engineering, Southern University of Science and Technology, Shenzhen 518055, China
[f] Shenzhen Research Institute, The Chinese University of Hong Kong, Shenzhen 518057, China
[g] Earth System Science Program, The Chinese University of Hong Kong, Hong Kong

ARTICLE INFO

Keywords:
Mariana trench
3-D plate bending
Numerical simulation
Yield zone depth
Earthquakes

ABSTRACT

Two tectonic plates converge at subduction zones where the subducting plate bends. Flexural bending of a subducting plate at a trench results in pervasive normal faulting, providing conduits for plate hydration and influencing the water budget and seismic behavior of the plate interface. 2-D plate bending simulations have demonstrated high strains due to strong bending may result in loss of strength of the lithosphere and intraplate earthquakes near the trench axis. However 3-D plate bending deformation may affect the along-strike slab pull force, especially when the deflection changes along the trench. Here we simulated the 3-D plate bending deformation and calculated bending stresses, and brittle failure of the Pacific plate at the Mariana Trench. We find that both the plate deflection and the yield zone depth (~16–20 km) increases from the northern to southern Mariana Trench. The water flux in the plate at the southern Mariana Trench is estimated to be about 15% greater than that of the northern Mariana Trench. By comparing with 2-D models, we further find that the 2-D approaches may underestimate the yield zone depth as they ignored the along-trench effects of plate deflection. The new results provide a self-consistent framework for interpretation of the observed surface normal faults, extensional earthquakes, and the inferred hydration of the subducting plate as constrained by seismic velocity anomalies.

1. Introduction

Flexural bending causes extensional brittle failure at the shallow part of a subducting plate (Watts, 2001). The resulting normal faulting can provide pathways for seawater to hydrate the crust and upper mantle prior to subduction (Ranero and Sallares, 2004; Rupke et al., 2004; Grevemeyer et al., 2007), thus their pervasiveness and depth extent strongly affect the water budget of a subducting plate (Faccenda et al., 2009). The hydration in turn influences the seismic behavior of the subduction plate interface (Ammon et al., 2008; Beaven et al., 2010; Lay et al., 2010). Furthermore, these normal faults can potentially generate devastating earthquakes and tsunamis (Lynnes and Lay, 1988; Yoshida et al., 1992; Lay et al., 2010). Plate bending and normal faulting have been comprehensively investigated in 2-D models (Ranero et al., 2003; Billen and Gurnis, 2005; Contreras-Reyes and Osses, 2010; Naliboff et al., 2013; Zhang et al., 2014; Zhou et al., 2015; Hunter and Watts, 2016; Zhou and Lin, 2018; Zhou et al., 2018). However, the 3-D characteristics of a subducting plate have been little investigated. Manríquez et al. (2014) presented a finite-element 3-D plate bending model of the Chile Trench. Garcia et al. (2019) provided an iterative spectral method for 3-D thin plate flexure with spatially variable rigidity. In this study, we focus on the following key issues: (1) What are the modes of 3-D deformation of a subducting plate? (2) How does the 3-D deformation relate to the observed local trench deeps, seamounts, surface normal faults, and earthquakes? (3) How do the yield zone, normal faulting, and water flux vary along a trench?

The 2,000-km-long Mariana Trench is an ideal natural laboratory for addressing the above science issues: (1) The depth of the Mariana Trench

* Corresponding authors at: Key Laboratory of Ocean and Marginal Sea Geology, South China Sea Institute of Oceanology, Innovation Academy of South China Sea Ecology and Environmental Engineering, Chinese Academy of Sciences, Guangzhou 510301, China.

E-mail addresses: zhangfan@scsio.ac.cn (F. Zhang), jlin@whoi.edu (J. Lin).

https://doi.org/10.1016/j.tecto.2021.228944
Received 6 January 2021; Received in revised form 11 May 2021; Accepted 18 May 2021
Available online 23 May 2021

varies significantly from south to north (Ryan et al., 2009; Weatherall et al., 2015) (Fig. 1a and Fig. S1a in the Supplementary material); (2) the age range of the Mariana subducting plate is relatively narrow (140–160 Ma), and thus the variation in the effective elastic plate thickness is not a first-order effect; (3) the Mariana Trench has been the focus of recent multiple seismic experiments (Cai et al., 2018; Wan et al., 2019); and (4) high-resolution bathymetry data are available for most of the Mariana Trench, providing direct constraints on the spatial variations in surface normal faults.

In this study, we developed one of the first 3-D bending analyses of the Pacific plate at the Mariana Trench. We first used a thin-plate approximation to model the vertical deformation of a 3-D elastic plate and then analyzed the depth variation in the extensional stresses and yielding of the plate. The calculated plate deformation was then compared with the observed surface normal faults and extensional earthquakes. Finally, we estimated the water flux and degree of serpentinization in the subducting Pacific plate, comparing the results with the shear-wave seismic velocity profiles. Together, these analyses provide new insights on the 3-D processes of a subducting plate.

2. Method

2.1. Flexural model and curvature calculation

We used the Kirchhoff-Love thin plate assumption (Timoshenko and Woinowsky-Krieger, 1959) to calculate the vertical deformation (w) of a 3-D thin plate (Wessel, 1996):

$$\nabla^2\left(D\nabla^2 w\right)\text{-}(1-\nu)\times\left(\frac{\partial^2 D}{\partial x^2}\frac{\partial^2 w}{\partial y^2}-2\frac{\partial^2 D}{\partial x\partial y}\frac{\partial^2 w}{\partial x\partial y}+\frac{\partial^2 D}{\partial y^2}\frac{\partial^2 w}{\partial^2 x^2}\right)\text{-}N_{xx}\frac{\partial^2 w}{\partial x^2}\text{-}2N_{xy}\frac{\partial^2 w}{\partial x\partial y}\text{-}N_{yy}\frac{\partial^2 w}{\partial y^2}+\Delta\rho g w=q(x,y) \tag{1}$$

where $q(x, y)$ is spatially varying vertical loading force; $\Delta\rho = \rho_m - \rho_w$ is the density contrast between the mantle and water; and g is the gravitational acceleration. N_{xx}, N_{xy}, and N_{yy} are the in-plane forces. The flexural rigidity D is given by$D = \frac{ET_e^{\,3}(x,y)}{12(1-\nu^2)}$, where E and ν represent the Young's modulus and Poisson's ratio, and T_e is the effective elastic thickness (Table 1). Unlike 2-D model in which the bending moment (M) and vertical shear stress (V) have simple forms, M and V in 3-D situation are given by:

$$\begin{aligned} M_x &= \text{-}D\left(\frac{\partial^2 w}{\partial x^2}+\nu\frac{\partial^2 w}{\partial y^2}\right)\\ M_y &= \text{-}D\left(\frac{\partial^2 w}{\partial y^2}+\nu\frac{\partial^2 w}{\partial x^2}\right)\\ M_{xy} &= \text{-}D(1\text{-}\nu)\frac{\partial^2 w}{\partial x\partial y}\end{aligned} \tag{2}$$

and

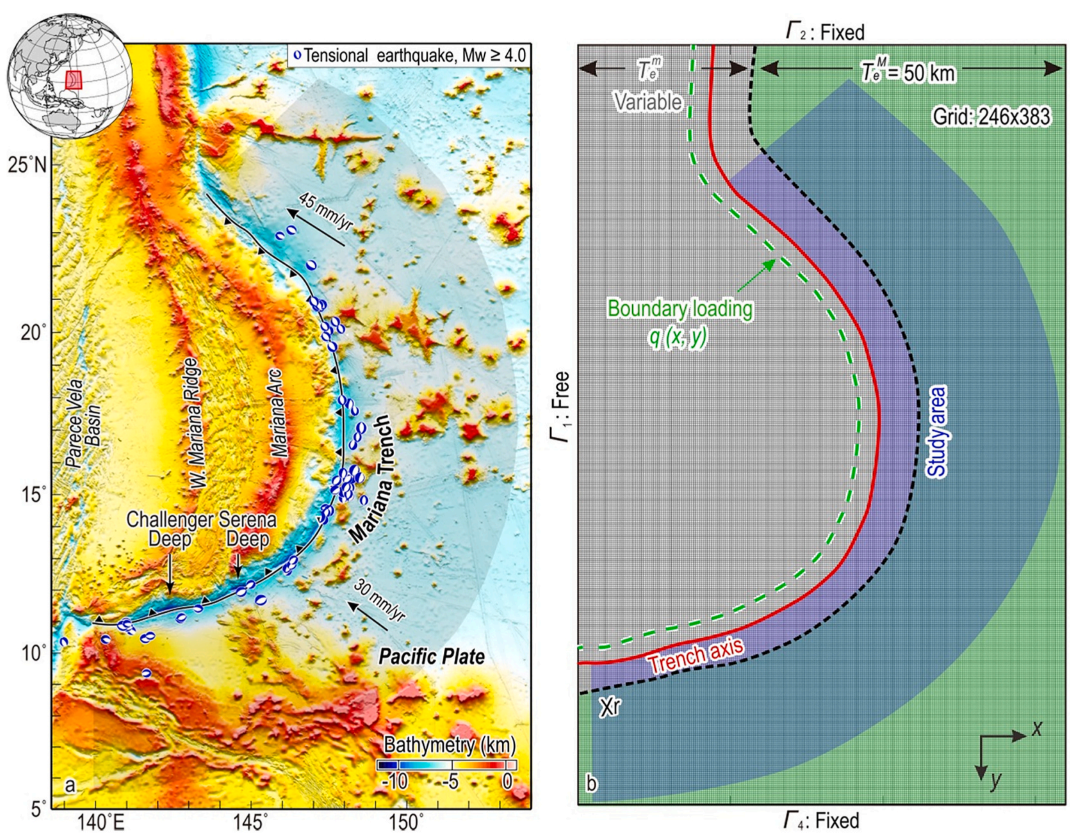

Fig. 1. (a) Topography of the Mariana Trench. The shaded area is the modeled subducting plate. The black arrows represent the subduction directions. The blue beach balls show the outer-rise extensional earthquakes of $Mw \geq 4.0$ recorded by the GCMT database. (b) Model setup. The grid size of the model is ~6.5 km, yielding a total of 246×383 grids. Red line marks the trench axis, which is subjected to a boundary loading $q(x, y)$ along the trench axis. Blue and purple color mark the areas with $T_e^M(x, y)$ and $T_e^m(x, y)$, respectively. Black dashed line indicates the breaking points between the T_e^M and T_e^m. Blue color marks the study area. The boundary Γ_1 is free boundary, while Γ_2, Γ_3, and Γ_4 are fixed.

Table 1
Parameters used in flexural analysis and the yield zone evenlope (Section 2.1 and 2.2)

Parameters	Description	Value	Unit
E	Young's modulus	7×10^{10}	Pa
g	Acceleration due to gravity	9.81	m/s^2
ν	Poisson's ratio	0.25	
ρ_m	Mantle density	3300	kg/m^3
ρ_c	Crust density	2700	kg/m^3
ρ_s	Sediment density	2000	kg/m^3
ρ_w	Water density	1030	kg/m^3
C_0	Cohesion	44	MPa
A	Pre-exponential	1.4×10^{-7}	s^{-1} MPa^{-n}
n	Stress exponent	2	
H_0*	Zero-stress activation enthalpy	320	kJ mol^{-1}
σ_P	Peierls stress or glide resistance	5.9	GPa
p,q	Geometry dependent parameters	½, 1	
B	A material-dependent parameter	1.10×10^5	$^{-1}$ MPa^{-n}
E*	Activation energy	530	kJ mol^{-1}
V*	Activation volume	14×10^{-6}	m^3 mol^{-1}

$$V_x = -\frac{\partial D}{\partial x}\left(\frac{\partial^2 w}{\partial x^2}+\nu\frac{\partial^2 w}{\partial y^2}\right)-2(1-\nu)\frac{\partial D}{\partial y}\frac{\partial^2 w}{\partial x\partial y}-D\left[\frac{\partial^3 w}{\partial x^3}+(2-\nu)\frac{\partial^3 w}{\partial x\partial y^2}\right]-N_x\frac{\partial w}{\partial x}-2N_{xy}\frac{\partial w}{\partial y}$$
$$V_y = -\frac{\partial D}{\partial y}\left(\frac{\partial^2 w}{\partial y^2}+\nu\frac{\partial^2 w}{\partial x^2}\right)-2(1-\nu)\frac{\partial D}{\partial x}\frac{\partial^2 w}{\partial x\partial y}-D\left[\frac{\partial^3 w}{\partial y^3}+(2-\nu)\frac{\partial^3 w}{\partial x^2\partial y}\right]-N_y\frac{\partial w}{\partial y}-2N_{xy}\frac{\partial w}{\partial x} \tag{3}$$

The equation (1) was solved by the finite-difference method (FDM) under different boundary conditions and surface loading (q(x, y)) (Fig. 1b). The model parameters are displayed in Table 1. The boundary conditions include following: stress free on the boundary Γ_1, while Γ_2, Γ_3 and Γ_4 are fixed. They are given by:

$$\begin{aligned}\Gamma_1 &: M=0, V=0,\\ \Gamma_2 &: w=0, M=0,\\ \Gamma_3 &: w=0, M=0,\\ \Gamma_4 &: w=0, M=0,\end{aligned} \tag{4}$$

Previous studies used trench-axis loading in the form of bending moment (M_0) and vertical shear force (V_0). The robustness and sensitivity of variable flexural parameters (M_0, V_0, and T_e) have been tested in 2-D (Zhang et al., 2014; Hunter and Watts, 2016) and 3-D cases (Zhang et al., 2019), respectively.

In this study, we used a more generic boundary loading form q, which represents synthetic loading and can adequately reproduce M_0 and V_0 numerically (Fig. S2 in the Supplementary material). Some previous studies suggested that T_e varies with plate age (Hunter and Watts, 2016; Zhang et al., 2018b), while other studies indicate little age dependence (Bry and White, 2007; Contreras-Reyes and Osses, 2010; Craig and Copley, 2014). In this study, for simplicity the T_e was divided into two parts: T_e^M and T_e^m seaward and trench-ward of the outer rise, respectively, breaking at a distance of X_r parallel to the trench axis (Fig. 1b). $T_e^M = 50$ km was set to be a constant (Zhang et al., 2014). The $q(x, y)$ and $T_e^m(x, y)$ vary freely along the trench axis. In order to avoid the potential edge effect of direct application of loading on the trench axis, the $q(x, y)$ was applied at a constant distance of 60 km (green dashed line) to the west of the trench axis. Note that only the region east of the trench axis (purple and green colors) is of physical meaning and of interest, while the region west of the trench axis (grey area) is fictious in the bending analysis and not of interest. Therefore, we only analyzed the predicted bending deformation in the study region (Fig. 1b). The grid size is ~6.5 km.

We aim to find a solution of combination of {q, T_e^m, X_r} to minimize the root mean square (RMS) difference W_{RMS} between the modeled deformation and the non-isostatic topography:

$$W_{RMS} = \sqrt{\frac{1}{n}\sum_{i=0}^{n}\left|w_i^{cal}-w_i^{obs}\right|^2} \tag{5}$$

n is the number of points of study area w^{obs} is the observation bathymetry data and w^{cal} is the calculated result using eq. (1). First, we used the previous 2-D thin plate model results (Zhang et al., 2014) to constrain the range of solution space of {q, T_e^m, X_r}. We then explored the solution space manually to seek solutions that are successively close to the observation until a deformation surface was obtained, which can capture the key features of the non-isostatic topography.

2.2. Calculation of extensional yield zone

Flexural bending of a subducting plate is expected to cause brittle yielding and plastic deformation in the upper and lower plates, respectively (Fig. 2a) based on the yield strength envelope (YSE) (Fig. 2c) (Byerlee, 1978; Garcia-Castellanos et al., 2000; Hunter and Watts, 2016). The maximum sustainable deviatoric stress at the upper plate was determined by the cohesion of the lithosphere C_0 (Fig. 2c, Table 1) (Lavier et al., 2000) and the maximum shear stress $\Delta\tau = \mu(\sigma_n - P_f)$, where μ, σ_n, and P_f are the rock frictional coefficient, normal stress, and pore fluid pressure on the fault planes, respectively. Plastic deformation at the lower plate is controlled by the temperature-dependent power-law rheology (Goetze, 1978; Goetze and Evans, 1979; Hirth and Kohlstedt, 2003; Mei et al., 2010; Hunter and Watts, 2016; Zhang et al., 2018a). In the ductile regime, combination of two ductile flow laws is adopted in our work (same as in Hunter and Watts, 2016). In the low-temperature regime, the ductile flow of low-temperature plasticity (LTP) is given by:

$$\dot{\varepsilon} = A\sigma^n\left\{-\frac{H_0^*}{RT}\left[1-\left(\frac{\sigma}{\sigma_P}\right)^p\right]^q\right\} \tag{6}$$

where $\dot{\varepsilon}$,σ, R, and T are the strain rate, differential stress, gas constant, and temperature, respectively. A is the pre-exponential determined by pressure, grain size, and volatile content. H_0* is the zero-stress activation enthalpy, n is a non-dimensional parameter and σ_P is the Peierls stress or glide resistance. p and q are geometry dependent parameters. The values of parameters in this study follow the work of Mei et al. (2010): $A = 1.4\times10^{-7}$ s^{-1} MPa^{-n}, $n = 2$, H_0* = 320 kJ mol^{-1}, $\sigma_P = 5.9$ GPa, p= ½, and q=1. The temperature structure is shown in Fig. 2b (Stein and Stein, 1992). At higher temperature (~600–800 °C), the ductile flow of power-law creep (PLC) is given by

$$\dot{\varepsilon} = B\sigma^n exp\left(-\frac{E^*+PV^*}{RT}\right) \tag{7}$$

where B is a material-dependent parameter, n is the stress exponent and E* is the activation energy, V* is the activation volume, P and T are pressure and temperature, respectively. The values of parameters in this study follow the work of Hirth and Kohlstedt (2003): $B = 1.10\times10^5$ s^{-1} MPa^{-n}, E* = 530 kJ mol^{-1}, and V* $=14\times10^{-6}$ m^3 mol^{-1}.

Following the work of Hunter and Watts (2016), we adopted the low-temperature rheology law of Mei et al. (2010) and the high-temperature rheology law of Hirth and Kohlstedt (2003), respectively. At the central depth, an elastic core is sandwiched between the upper brittle yield zone and the lower layer of plastic deformation (Fig. 2a). The deviatoric stress (Fig. 2c) in the elastic core was calculated by $\Delta\sigma_{xx}^{elastic} = \frac{E(z-z_n)k}{1-\nu^2}$, where z presents the distance from the neutral plane, z_n is the depth of the neutral plane, and k is the maximum plate deformation curvature which is the function of (x, y) in 3-D situation (Please see the section 2.3). The brittle yield zone was then determined by the maximum sustainable deviatoric stress and curvature of the flexural bending plate. Additional details of the calculation methods were described in Zhang et al., 2020a; Zhang et al., 2020b. All parameters used in flexural analysis are displayed in the Table 1.

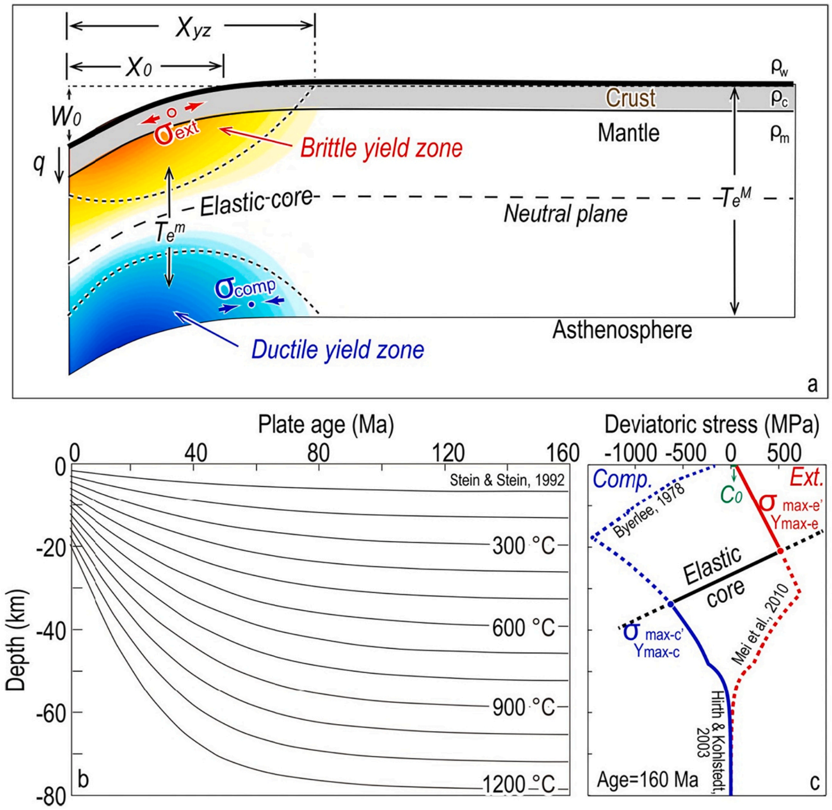

Fig. 2. (a) Schematic model of a subducting plate. The key bending parameters include the following: q is the vertical loading force; X_0 represents the location where the vertical deformation $w = 0$; X_{yz} represents the width of the yield zone; and T_e^M and T_e^m are the effective elastic plate thickness seaward of the outer-rise region and at the trench axis, respectively. The upper and lower parts of the plate near the trench are associated with the brittle yield zone (orange) and the ductile yield zone (blue), respectively. (b) Plate cooling model (Stein and Stein, 1992) (c) Deviatoric stress as a function of depth at the trench axis (Byerlee, 1978; Hirth and Kohlstedt, 2003; Mei et al., 2010). The blue and red curves represent the yield strength envelope (YSE) and the black line shows the slope of the elastic core.

2.3. Maximum curvature of plane

For 2-D models, the deviatoric stress can be calculated from the curvature along the profile (Please see the Section 2.2), while in the 3-D situation, the deviatoric stress should be calculated from the maximum curvature of plane (Garcia et al., 2019). According to the theory of differential geometry, the two principal curvatures at a given point on a surface measure how a surface bends in different directions at that point. If a surface $w(x, y)$ has continuous second-order partial derivatives, it could be described by the first and second fundamental forms of the surface:

$$\begin{aligned} S_1 &= E_p dx^2 + 2F_p dxdy + G_p dy^2 \\ S_2 &= L_p dx^2 + 2M_p dxdy + N_p dy^2 \end{aligned} \tag{8}$$

where E_p, F_p and G_p are first basic parameters and L_p, M_p and N_p are second basic parameters. The normal curvature of any point (u, v) on a surface is given by

$$k_n = \frac{S_2}{S_1} = \frac{L_p du^2 + N_p dv^2}{E_p du^2 + G_p dv^2} \tag{9}$$

Assuming that k_1 and k_2 are the maximum and minimum of the normal curvature k, they can be described by

$$\begin{aligned} &\left(E_pG_p\text{-}F_p{}^2\right)k^2\text{-}\left(L_pG_p\text{-}2M_pF_p + N_pE_p\right)k + \left(L_pN_p\text{-}M_p{}^2\right) = 0, \\ &(k_1, k_2) = \left(B \pm \sqrt{B^2\text{-}4AC}\right)\Big/(2A), \\ &A = E_pG_p\text{-}F_p{}^2, B = L_pG_p\text{-}2M_pF_p + N_pE_p, C = L_pN_p\text{-}M_p{}^2, \end{aligned} \tag{10}$$

In the thin plate model, the first-order partial derivative can be omitted and thus E_p, F_p, G_p, L_p, M_p, and N_p can be described as:

$$\begin{aligned} &E_p = 1;\ \ F_p = 0;\ \ G_p = 1 \\ &L_p = \frac{\partial^2 w}{\partial x^2};\ \ M_p = \frac{\partial^2 w}{\partial x \partial y};\ \ N_p = \frac{\partial^2 w}{\partial y^2} \end{aligned} \tag{11}$$

where k_{xx}, k_{yy} and k_{xy} represent the second partial derivatives of the flexure of subducting plate The maximum (k_1) and minimum (k_2) curvatures are given as:

$$(k_1, k_2) = \frac{1}{2}\left(k_{xx} + k_{yy}\right) \pm \sqrt{\frac{1}{4}\left(k_{xx}\text{-}k_{yy}\right)^2 + k_{xy}{}^2} \tag{12}$$

All definitions of symbols used in the calculateion of plate maximum curvature are displaye in the Table 2.

3. Results

3.1. 3-D flexural bending and curvature

The flexural bending deformation (Fig. 3) was obtained by comparison with the observed non-isostatic topography of the Mariana Trench (Zhang et al., 2014) (Fig. S1b). The overall deformation pattern

Table 2
Illustration of symbols in calculation of plate maximum curvature (Section 2.3)

Symbol	Description
E_p	The coefficient of the first term in the first fundamental formula of the plane
F_p	The coefficient of the second term in the first fundamental formula of the plane
G_p	The coefficient of the third term in the first fundamental formula of the plane
L_p	The coefficient of the first term in the second fundamental formula of the plane
M_p	The coefficient of the second term in the second fundamental formula of the plane
N_p	The coefficient of the third term in the second fundamental formula of the plane
k_n	Normal curvature of the plane
k_1	The maximum curvature of the plane
k_2	The minimum curvature of the plane

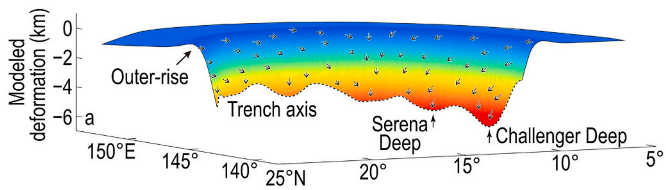

Fig. 3. 3-D modeling of the flexural bending of the subducting Pacific plate at the Mariana Trench. The color represents the depth. Red is deep and blue is shallow. The black dashed curve represents the trench axis. The black arrows show the maximum curvature directions.

is also consistent with the variation in the free-air gravity anomaly (Sandwell et al., 2014) (Fig. S1c). The modeled trench relief W_0 ranges from 2.4 to 6.2 km along the trench axis, with RMS value of ~164 m between the model and observation along the trench axis (Fig. 4a and Table S1 in the Supplementary material). The calculated W_0 shows an increase in the deformation toward the Challenger Deep (at along-trench distance of 0–300 km) and then a northward decrease in the deformation (at along-trench distance of 300–2,300 km) (Figs. 3 and 4a). The calculated trench width (X_0) (Fig. 2) also varied significantly, ranging from 36 to 86 km (Table S1 in the Supplementary material). The maximum flexural bending curvature of the subducting Pacific plate was largest near the trench axis and decreased away from the trench axis. The maximum curvature at the trench axis (K_0) varied between 0.12 and

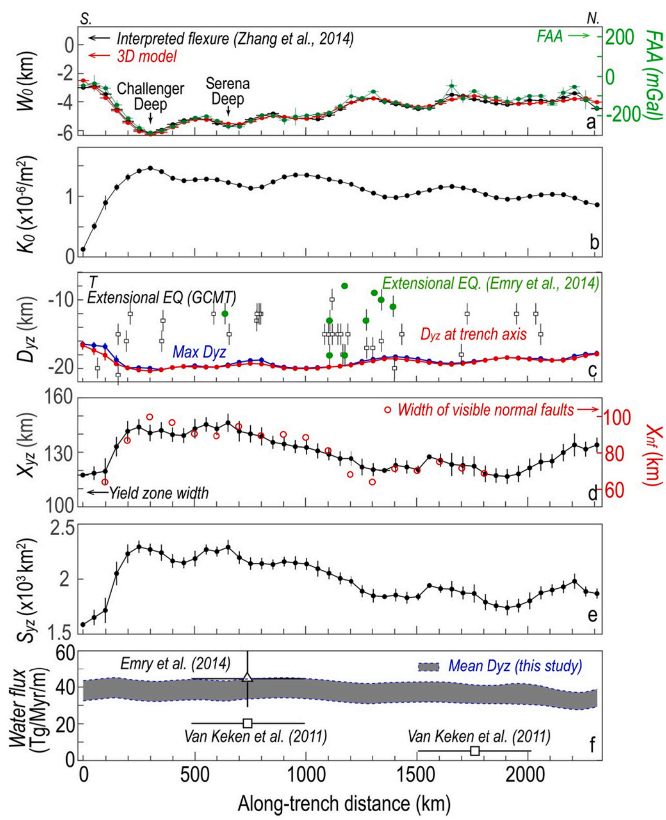

Fig. 4. The along-trench variations in bending parameters. (a) Interpreted (black curve) and modeled (red curve) flexural bending; Free-air gravity anomaly (green curve); (b) Maximum curvature; (c) Maximum yield zone depth at the trench axis. Black squares mark the outer-rise extensional earthquakes of $Mw \geq 4.0$ recorded by the GCMT database. Green circles mark the relocated earthquakes; (d) Width of yield zone and width of the visible surface normal faults; (e) Area of yield zone; and (f) Estimated average water flux of five segments of the Mariana Trench using the mean D_{yz} minus the mean crustal thickness. The partial serpentinization is assumed to be with 2 wt% H_2O. Black lines mark the results from previous studies.

1.46×10^{-6} m^{-1} (Figs. 4b and 5a). The southern Mariana Trench had relatively large values of K_0 (Fig. 4b), indicating relatively strong flexural bending in comparison to the northern and central Mariana Trench (Figs. 4a).

3.2. 3-D stress distribution and failure zone

We calculated the 3-D deviatoric stress and corresponding yield zone along the Mariana Trench (Table S1 in the Supplementary material). The maximum extensional deviatoric stresses were found in the trench axis of the Challenger Deep ($\sigma_{xx\text{-}e}$ = 505 MPa), together with the maximum depth of the extensional yield zone (D_{yz} = 20.4 km) (Table S1). The maximum extensional deviatoric stresses ($\sigma_{xx\text{-}e}$) at the trench axis were 395–505 MPa (Table S1 in the Supplementary material) and at depths (D_{yz}) of 16.6–20.4 km (Figs. 4c and 5b, Table S1 in the Supplementary material). The bending curvature decreases to a negligible value (0.1×10^{-6} m^{-1}) at a characteristic distance (X_{yz}) of 116–146 km, which was defined as the yield zone width (Figs. 4d, Table S1 in the Supplementary material). A similar trend was found in the observed width of the visible surface normal faults from the analysis of the multi-beam bathymetry data (Fig. 5c). The corresponding total yield zone area (S_{yz}) was in the range of 1,587–2,298 km^2 (Fig. 4e and Table S1 in the Supplementary material), which we interpreted as the size of the potential serpentinization zone. The size of the potential serpentinization zone of the southern Mariana Trench was found to be ~1.3 times that of the northern Mariana Trench (Fig. 4e).

4. Discussion

4.1. 3-D effects on plate bending

We identified three types of 3-D effects on plate bending, which were little investigated in previous 2-D studies (Figs. S3 and S4 in the Supplementary material). First, because the 2-D model fails to consider the lateral effect of plate deflection and the direction the 2-D profile may not reflect the bending direction of the plate, the 2-D solutions underestimated the yield zone depth (D_{yz}) by up to ~30% for the geometry studied (Figs. S3d and S4d in the Supplementary material). Second, the equation of 2-D elastic model implies a assumption that loads keep constant along the strike of trench. 3-D model can better illustrate the reality by considering the along-strike loading. Third, in the 3-D model, loading at a given point at the trench axis (Fig. S4a in the Supplementary material) can influence deformation within an along-axis distance of L_i (Figs. S4b-d in the Supplementary material). Such a 3-D influence distance (L_i) is found to increase with the T_e (Fig. S4e in the Supplementary material). Our calculated yield zones from our 3-D elastic models are close to that of the 2-D elasto-plastic models (Zhou et al., 2018) (Fig. S5 in the Supplementary material). Along the Mariana trench, the T_e at the trench axis ranges in ~18-40 km (Zhou et al., 2018), corresponding to the lateral 3-D influence distance of ~95-270 km (Fig. S4e in the Supplementary material).

We built a test model to illustrate the difference on estimating bending stress between 2-D and 3-D model under along-strike variable loading (V_0) (Fig. S6 in the Supplementary material). In the test model, V_0 changes from V_0^1 to V_0^2 linearly within a distance L along strike, and the T_e is set to a constant value (35 km) (Fig. S6a in the Supplementary material). We carry out 21 different calculation models in which the ratio V_0^2/V_0^1 and L/L_m are set to different values (every red dot in Fig. S6d represents one model). We then find that the changes in both V_0 and the variation distance L (we used L/L_m in Fig. S6d, where L_m is the width of our model) can affect the results, in which the bending stress increases with V_0 and decreases with L (Fig. S6d in the Supplementary material).

Seismologists are concern about the effect of material parameters (such as the Young's modulus: E) of plate on plate deformation. We designed a model to investigate the impact of E on plate deflection and bending elastic stress (Fig. S7). it shows that with increase of E, the plate

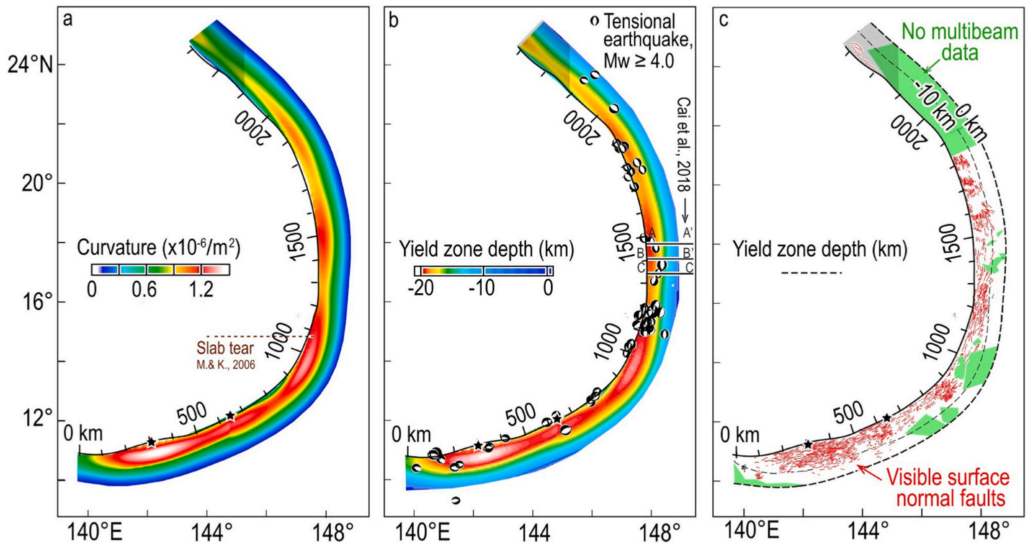

Fig. 5. (a) Calculated curvature; and (b) yield zone depth of the Pacific subducting plate. Here the yield zone depth means the bottom depth of brittle yield zone (Fig. 2a). Black beach balls represent the normal faulting earthquakes along the Mariana Trench. (c) Yield zone depth contour and surface normal faults identified from the high-resolution topography. Area without good constraints was shaded. Green areas mark the regions without multi-beam bathymetry data. The brown dashed lines show the locations of the slab tears proposed by Gvirtzman and Stern (2004), Miller and Kennett (2006).

deflection becomes smaller while the maximum of bending stress become larger (Fig. S7a). The variation rates of both plate deflection and maximum of bending stress decreases with E (Fig. S7b). This means that for a subducting plate, larger E may causes a deeper area where bending-related normal earthquakes occur.

4.2. Comparison with observed faults, earthquakes, and seismic profiles

We compared the calculated width of yield zone (X_{yz}) (Fig. 4d) and the observed surface normal faults (Fig. 5c). Some of normal faults at the outer-rise might not be shown in the bathymetry data because they are too small. Overall, the measured width of the visible surface normal faults is smaller than the calculated X_{yz}. Neverthless, the along-trench variation in the X_{yz} (Fig. 4d) corresponds relatively well with the width of the measured visible surface normal faults (Fig. 5c). The calculated depth of the brittle yield zone was also comparable with the observed seismicity data (Fig. 4c). A total of 66 $Mw \geq 4.0$ normal faulting earthquakes (-135° < rake < -45°) during 1976-2020 were located in the outer-rise region of the Mariana Trench (GCMT, http://www.globalcmt.org). Most of these normal faulting events have strikes that were sub-parallel to the trench axis, within 150 km from the trench axis (Fig. 5b), and at a depth of 10–33 km (Fig. 4c). Nighty-five percent (63 out of 66) of the normal faulting earthquakes occurred within the calculated 3-D brittle yield zone (Figs. 4c, 5b, and 6). Most of the relocated normal faulting earthquakes by Emry et al. (2014) were also within the calculated brittle yield zone (Figs. 4c and 6). Our results overall match the depths of outer rise earthquakes from GCMT and Emry et al. (2014). Eimer et al. (2020) showed that extensional earthquake occurs to depth of 31km below the seafloor, which is deeper than our

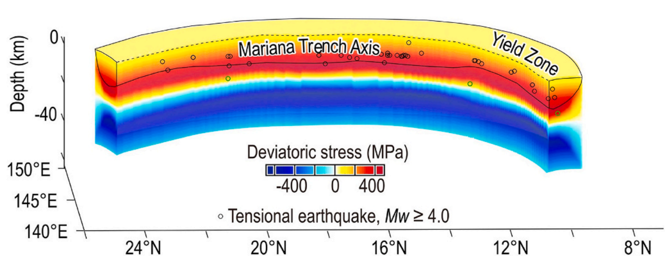

Fig. 6. 3-D distribution of the deviatoric stress in the Pacific subducting plate. The black and green circles represent the outer-rise $Mw \geq 4.0$ extensional earthquakes within (black circle) and outside (green circle) of the calculated yield zone, respectively.

results. This may be correlated with the regional stress which is not considered in this study, as outer-rise stress environment depends not only on the plate bending, but also on locking and unlocking of the interplate. Therefore, we suggest that the regional stress (such as frictional resistance on the interplate fault) should be considered in the further works. Furthermore, the calculated yield zone shape also matches relatively well with the shear-wave seismic velocity contour of 3.9 km/s (V_s) (Cai et al., 2018), which was suggested to correspond to the boundary of a partial serpentinization zone in the mantle (Figs. 5b and 7).

4.3. Water flux estimation

The bending-induced normal faults provide significant pathways for water to enter the crust and uppermost mantle, enhancing partial serpentinization of the subducting slab. A portion of the water contained in the sediment and oceanic crust is released at shallow depth, whereas the amount of water carried into the deeper mantle can be estimated by the amount of mantle serpentinization of the subducting plate (Emry et al., 2014). Previous studies have estimated the downgoing water flux of the global subduction zones by considering the serpentinized mantle as a homogeneous layer with different subduction rate, such as 4.7cm/yr (Jarrard, 2003), 4.1 cm/yr (Hacker, 2008) and 5.0cm/yr (Van Keken et al., 2011). Along the southern Mariana Trench, Van Keken et al. (2011) estimated 21.2 Tg/Myr/m for partial serpentinization of the upper 2 km of the mantle. Emry et al. (2014) calculated ~15–30 Tg/Mry/m of downgoing water flux along the southern-central Mariana Trench at ~15°–20°N, assuming the depth of the extensional earthquakes in the outer-rise region corresponded to the depth of the mantle serpentinization. At the northern Mariana Trench, Van Keken et al. (2011) estimated 6.5 Tg/Myr/m for partial serpentinization (Fig. 4f).

In our model, the maximum depth of the yield zone varied in the range of ~16–20 km with an average depth of ~18.5–19.5 km from the northern to southern Mariana Trench (Fig. 4c). Along the Mariana Trench, the subducting crust has an average thickness of ~6–7 km (Van Keken et al., 2011). Therefore, the average depth of the mantle serpentinization below the Moho was estimated to be in the range of ~8–13 km. Following the same assumption of moderate hydration of the upper mantle as in previous studies (Van Keken et al., 2011; Emry et al., 2014), we assumed the degree of the partial serpentinization to be in the range of 1.5–2 wt% H_2O, and calculated the average water flux using the mean D_{yz} minus the mean crustal thickness. The resulting average water flux in the southern Mariana Trench was ~34.5–44 Tg/Myr/m, which is about 15% greater than that of the northern Mariana Trench (~28–38.8 Tg/

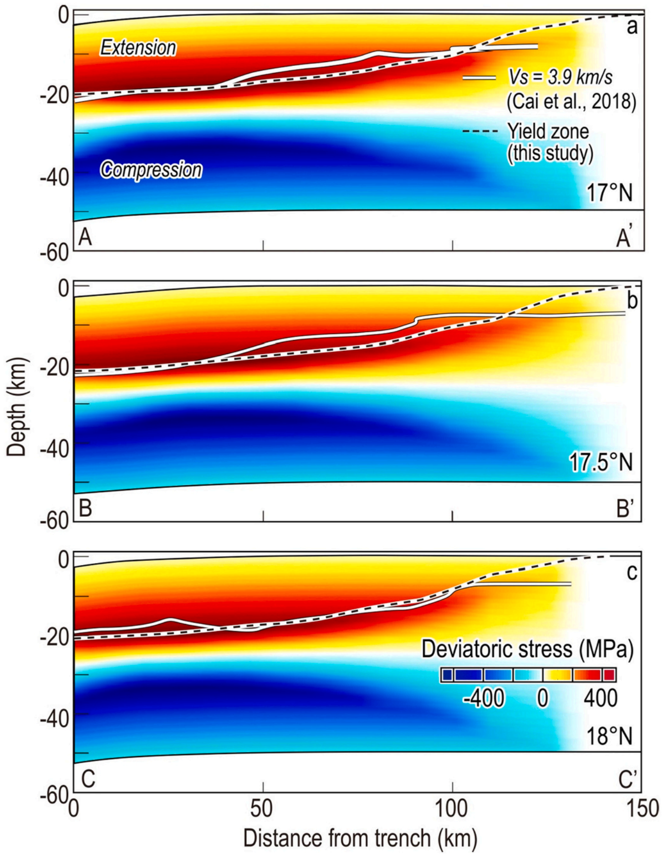

Fig. 7. Comparison of the calculated yield zone with area of part serpentinization and pore water of across-trench profiles shown in Fig. 5b. The black dashed curves mark the bottom of the extensional yield zone in our model. The white curves mark the velocity contours of 3.9 km/s (V_s) (Cai et al., 2018), which is interpreted as area of partial serpentinization in the mantle and pore-water infiltration in the crust.

Myr/m) (Fig. 4f, Table 3). Our results are very close to that of Emry et al. (2014) and about ~2–2.5 times that of Van Keken et al. (2011) (Fig. 4f, Table 3). In the central Mariana Trench at 16°–18°N, our estimation of 31–42 Tg/Myr/m is nearly half of that of Cai et al. (2018) (~79±17 Tg/Myr/m). The difference may come from the fact that Cai et al. (2018) assumed a 24 km thick partially serpentinized layer with 2 wt% water, however our results give a variable-thickness serpentinized layer.

5. Conclusions

By analyzing the plate deflection, stresses, and brittle failure of the subducting plate along the Mariana trench, we draw the following conclusions:

1. The depth of the calculated yield zone varies in the range of ~16–20 km from the northern to southern Mariana Trench. The corresponding water flux in the southern Mariana Trench is estimated to be about 15% greater than that of the northern Mariana Trench.
2. When plate deflection varies along the strike of trench, 3-D effect plays an important role in estimating the trench-axis loading, plate bending stress and yield zone. The difference between 3-D and 2-D result can reach ~30%.
3. The calculated yield zone is consistent with the observed surface normal faults, extensional earthquakes, and the inferred hydration of the subducting plate constrained by seismic velocity anomalies.

Table 3
Estimated water flux along the Mariana Trench

Along-trench distance (km)	Water flux from Max. D_{yz} (Tg/Myr/m)	Water flux from mean D_{yz} (Tg/Myr/m)
0-500	58.6±1.8	44.6±1.4
500-1,000	57.3±0.4	41.8±1.4
1,000-1,500	55.2±1.0	38.8±1.3
1,500-2,000	51.3±1.8	34.8±1.3
2,000-2,300	45.0±3.3	30.2±2.5

- Water flux from Max. D_{yz} means the water flxu estimated by the maximum yield zone depth (D_{yz})
- Water flux from mean D_{yz} means the water flxu estimated by the mean yield zone depth (D_{yz})

Declaration of Competing Interest

None.

Acknowledgements

This research benefited from discussion with Drs. Xubo Zhang, Yen Joe Tan, and the SCSIO Marine Geodynamics Group. This work was supported by the Southern Marine Science and Engineering Guangdong Laboratory (Guangzhou) grant GML2019ZD0205; NSFC grants 41976064, 91958211, 41890813, and 91858207; the Chinese Academy of Sciences grants Y4SL021001, QYZDY-SSW-DQC005, 133244KYSB20180029, and 131551KYSB20200021; Hong Kong Research Grant Council Grants (No. 14304820, 14306119), Faculty of Science at CUHK; China Postdoctoral Science Foundation grant 2019M663119; and the National Key Research and Development Program of China grants 2018YFC0309800 and 2018YFC0310105.

Appendix A. Supplementary data

Supplementary data to this article can be found online at https://doi.org/10.1016/j.tecto.2021.228944.

References

Ammon, C.J., Kanamori, H., Lay, T., 2008. A great earthquake doublet and seismic stress transfer cycle in the central Kuril islands. Nature 451, 561–566. https://doi.org/10.1038/nature06521.

Beaven, J., Wang, X., Holden, C., Wilson, K., Power, W., Prasetya, G., Bevis, M., Kautoke, R., 2010. Near-simultaneous great earthquakes at Tongan megathrust and outer rise in September 2009. Nature 466, 959–963. https://doi.org/10.1038/nature09292.

Billen, M.I., Gurnis, M., 2005. Constraints on subducting plate strength within the Kermadec trench. J. Geophys. Res. 110, B05407 https://doi.org/10.1029/2004JB003308.

Bry, M., White, N., 2007. Reappraising elastic thickness variation at oceanic trenches. J. Geophys. Res. 112 https://doi.org/10.1029/2005JB004190.

Byerlee, J., 1978. Friction of rocks. Pure Appl. Geophys. 116 (4-5), 615–626. https://doi.org/10.1007/978-3-0348-7182-2_4.

Cai, C., Wiens, D.A., Shen, W., Eimer, M., 2018. Water input into the Mariana subduction zone estimated from ocean-bottom seismic data. Nature 563, 389–392. https://doi.org/10.1038/s41586-018-0655-4.

Contreras-Reyes, E., Osses, A., 2010. Lithospheric flexure modelling seaward of the Chile trench: implications for oceanic plate weakening in the Trench Outer Rise region. Geophys. J. Int. 182, 97–112. https://doi.org/10.1111/j.1365-246X.2010.04629.x.

Craig J., T., Copley, A., 2014. An explanation for the age independence of oceanic elastic thickness estimates from flexural profiles at subduction zones, and implications for continental rheology. Earth Planet. Sci. Lett. 392, 207–216. https://doi.org/10.1016/j.epsl.2014.02.027.

Eimer, M., Wiens, D.A., Cai, C., Lizarralde, D., Jasperson, H., 2020. Seismicity of the incoming plate and forearc near the Mariana Trench recorded by ocean bottom seismographs. Geochem. Geophys. Geosyst. 21 https://doi.org/10.1029/2020GC008953 e2020GC008953.

Emry, E.L., Wiens, D.A., Garcia-Castellanos, D., 2014. Faulting within the Pacific plate at the Mariana Trench: Implications for plate interface coupling and subduction of hydrous minerals. J. Geophys. Res. 119, 3076–3095. https://doi.org/10.1002/2013JB010718.

Faccenda, M., Gerya, T.V., Burlini, L., 2009. Deep slab hydration induced by bending related variations in tectonic pressure. Nat. Geosci. 2, 790–793. https://doi.org/10.1038/ngeo656.

Garcia, E.S., Sandwell, D.T., Bassett, D., 2019. Outer trench slope flexure and faulting at Pacific basin subduction zones. Geophys. J. Int. 218, 708–728. https://doi.org/10.31223/osf.io/dbn8j.

Garcia-Castellanos, D., Torne, M., Fernandez, M., 2000. Slab pull effects from a flexural analysis of the Tonga and Kermadec trenches (Pacific Plate). Geophys. J. Int. 141 (2), 479–484. https://doi.org/10.1046/j.1365-246x.2000.00096.x.

Goetze, C., 1978. The mechanisms of creep in olivine. Philosophical Transactions of the Royal Society A Mathematical Physical Engineering Scienc, A 288, 99–119. https://doi.org/10.1098/rsta.1978.0008.

Goetze, C., Evans, B., 1979. Stress and temperature in the bending lithosphere as constrained by experimental rock mechanics. Geophys. J. Roy. Astron. Soc. 59, 463–478. https://doi.org/10.1111/j.1365-246X.1979.tb02567.x.

Grevemeyer, I., Ranero, C.R., Flueh, E.R., Klaschen, D., Bialas, J., 2007. Passive and active seismological study of bending-related faulting and mantle serpentinization at the Middle America trench. Earth Planet. Sci. Lett. 258, 528–542. https://doi.org/10.1016/j.epsl.2007.04.013.

Gvirtzman, Z., Stern, R.J., 2004. Bathymetry of Mariana trench-arc system and formation of the Challenger Deep as a consequence of weak plate coupling. Tectonics 23, TC2011. https://doi.org/10.1029/2003TC001581.

Hacker, B.R., 2008. H_2O subduction beyond arcs. Geochem. Geophys. Geosyst. 9, Q03001 https://doi.org/10.1029/2007GC001707.

Hirth, G., Kohlstedt, D., 2003. Rheology of the upper mantle and the mantle wedge: a view from the experimentalists. Inside the Subduction Factory. Geophysical Monograph Series 138, 83–105. https://doi.org/10.1029/138GM06.

Hunter, J., Watts, A.B., 2016. Gravity anomalies, flexure and mantle rheology seaward of circum-Pacific trenches. Geophys. J. Int. 207, 288–316. https://doi.org/10.1093/gji/ggw275.

Jarrard, R.D., 2003. Subduction fluxes of water, carbon dioxide, chlorine, and potassium. Geochem. Geophys. Geosyst. 4, 8905. https://doi.org/10.1029/2002GC000392.

Lavier, L.L., Buck, W.R., Poliakov, A.N., 2000. Factors controlling normal fault offset in an ideal brittle layer. J. Geophys. Res. 105, 23,431–23,442. https://doi.org/10.1029/2000JB900108.

Lay, T., Ammon, C.J., Kanamori, H., Rivera, L., Koper, K.D., Hutko, A.R., 2010. The 2009 Samoa-Tonga great earthquake triggered doublet. Nature 466, 964–967. https://doi.org/10.1038/nature09214.

Lynnes, C., Lay, T., 1988. Source process of the great 1977 Sumba earthquake. J. Geophys. Res. 93, 13,407–14,320. https://doi.org/10.1029/JB093iB11p13407.

Manríquez, P., Contreras-Reyes, E., Osses, A., 2014. Lithospheric 3-D flexure modelling of the oceanic plate seaward of the trench using variable elastic thickness. Geophys. J. Int. 196, 681–683. https://doi.org/10.1093/gji/ggt464.

Mei, S., Suzuki, A.M., Kohlstedt, D.L., Dixon, N.A., Durham, W.B., 2010. Experimental constraints on the strength of the lithospheric mantle. J. Geophys. Res. 115 (B8) https://doi.org/10.1029/2009JB006873.

Miller, M.S., Kennett, B.L.N., 2006. Three-dimensional visualization of a near-vertical slab tear beneath the southern Mariana arc. Geochem. Geophys. Geosyst. 7 https://doi.org/10.1029/2005GC001110.

Naliboff, J.B., Billen, M.I., Gerya, T., Saunders, J., 2013. Dynamics of outer-rise faulting in oceanic-continental subduction systems. Geochem. Geophys. Geosyst. 14, 2310–2327. https://doi.org/10.1002/ggge.20155.

Ranero, C.R., Sallares, V., 2004. Geophysical evidence for hydration of the crust and mantle of the Nazca plate during bending at the north Chile trench. Geology 32, 549–552. https://doi.org/10.1130/G20379.1.

Ranero, C.R., Morgan, J.P., Mclntosh, K., Rsichert, C., 2003. Bending-related faulting and mantle serpentinization at the Middle America trench. Nature 425, 367–373. https://doi.org/10.1038/nature01961.

Rupke, L.H., Morgan, J.P., Hort, M., Connolly, J.D.L., 2004. Serpentine and the subduction zone water cycle. Earth Planet. Sci. Lett. 223, 17–34. https://doi.org/10.1016/j.epsl.2004.04.018.

Ryan, W.B.F., Carbotte, S.M., Coplanet, J.O., et al., 2009. Global Multi-Resolution Topography synthesis. Geochem. Geophys. Geosyst. 10, Q03014 https://doi.org/10.1029/2008GC002332.

Sandwell, D.T., Müller, R.D., Smith, W.H.F., Garcia, E., Francis, R., 2014. New global marine gravity model from CryoSat-2 and Jason-1 reveals buried tectonic structure. Science 346, 65–67. https://doi.org/10.1126/science.1258213.

Stein, C.A., Stein, S., 1992. A model for the global variation in oceanic depth and heat flow with lithospheric age. Nature 359, 123–129. https://doi.org/10.1038/359123a0.

Timoshenko, S., Woinowsky-Krieger, S., 1959. Theory of plates and shells, 2nd edition. New York, McGraw-Hill Press. 591 pp.

Van Keken, P.E., Hacker, B.R., Syracuse, E.M., Abers, G.A., 2011. Subduction factory: 4. Depth-dependent flux of H_2O from subducting slabs worldwide. J. Geophys. Res. 116, B01401. https://doi.org/10.1029/2010JB007922.

Wan, K., Lin, J., Xia, S., Sun, J., Xu, M., Yang, H., Zhou, Z., Zeng, X., Cao, J., Xu, H., 2019. Deep seismic structure across the southernmost Mariana Trench: Implications for arc rifting and plate hydration. J. Geophys. Res. 124, 4710–4727. https://doi.org/10.1029/2018JB017080.

Watts, A.B., 2001. Isostasy and flexure of the lithosphere. Cambridge University Press, New York, 458 pp.

Weatherall, P., Marks, K.M., Jakobsson, M., et al., 2015. A new digital bathymetric model of the world's oceans. Earth Space Sci. 2, 331–345. https://doi.org/10.1002/2015EA000107.

Wessel, P., 1996. Analytical solutions for 3-D flexural deformation of semi-infinite elastic plates. Geophys. J. Int. 124, 907–918. https://doi.org/10.1111/j.1365-246X.1996.tb05644.x.

Yoshida, Y., Satake, K., Abe, K., 1992. The large normal-faulting Mariana Earthquake of April 5, 1990 in uncoupled subduction zone. Geophys. Res. Lett. 19 (3), 297–300. https://doi.org/10.1029/92GL00165.

Zhang, J., Xu, M., Sun, Z., 2020a. Lithospheric flexural modeling of the seaward and trenchward of the subducting oceanic plates. Int. Geol. Rev. 62, 908–923. https://doi.org/10.1080/00206814.2018.1550729.

Zhang, F., Lin, J., Zhan, W., 2014. Variations in oceanic plate bending along the Mariana trench. Earth Planet. Sci. Lett. 401, 206–214. https://doi.org/10.1016/j.epsl.2014.05.032.

Zhang, F., Lin, J., Zhou, Z., Yang, H., Zhan, W., 2018a. Intra- and inter-trench variations in flexural bending of the Manila, Mariana and global trenches: Implications on plate weakening in controlling trench dynamics. Geophys. J. Int. 212, 1419–1449. https://doi.org/10.1093/gji/ggx488.

Zhang, J., Sun, Z., Xu, M., Yang, H., Zhang, Y., Li, F., 2018b. Lithospheric 3-D flexural modelling of subducted oceanic plate with variable effective elastic thickness along Manila Trench. Geophys. J. Int. 215, 2071–2092. https://doi.org/10.1093/gji/ggy393.

Zhang, F., Lin, J., Zhou, Z., 2019. Intra-trench variations in flexural bending of the subducting Pacific Plate along the Tonga-Kermadec Trench. Acta Oceanol. Sin. 38, 81–90. https://doi.org/10.1007/s13131-019-1493-4.

Zhang, F., Lin, J., Zhou, Z., 2020b. Flexural bending curvature and yield zone of subducting plates. Int. Geol. Rev. 62, 859–886. https://doi.org/10.1080/00206814.2019.1671237.

Zhou, Z., Lin, J., 2018. Elasto-plastic deformation and plate weakening due to normal faulting in the subducting plate along the Mariana Trench. Tectonophys. 734-735, 59–68. https://doi.org/10.1016/j.tecto.2018.04.008.

Zhou, Z., Lin, J., Behn, M.D., Olive, J.-A., 2015. Mechanism for normal faulting in the subducting plate at the Mariana Trench. Geophys. Res. Lett. 42, 4309–4317. https://doi.org/10.1002/2015GL063917.

Zhou, Z., Lin, J., Zhang, F., 2018. Modeling of normal faulting in the subducting plates of the Tonga, Japan, Izu-Bonin, and Mariana trenches: Implications for near-trench plate weakening. Acta Oceanol. Sin. 11, 53–60. https://doi.org/10.1007/s13131-018-1146-z.